CHANDRA
X-ray Center 60 Garden St., Cambridge Massachusetts 02138 USA

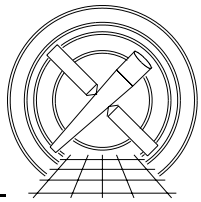

MEMORANDUM

Date: July 11, 2002
From: Beth Biller, Diab Jerius
To:
Subject: Measurement of Vignetting from G21.5 Observations
Re:
Cc:
File: `G21.5_memo.tex`
Version: `3.3`

Abstract

We measured vignetting as a function of off-axis angle θ normalized by on-axis vignetting. We used G21.5, a bright, non-piled up supernova remnant, as our test source. G21.5 was observed at 6 different off-axis angles ($0'$, $2'$, $5'$, $10'$, $15'$, $20'$, corresponding to obsids 1838-1843) for $\sim$8 ksec each. The $15'$ and $20'$ observations and half of the $5'$ observation had to be discarded due to background flaring. For each usable observation, we created a series of exposure maps for 1 keV bins in the 0-10 keV energy band. Exposure maps were weighted using a spectral fit to the on-axis observation. Backgrounds extracted $5'$ off-source were subtracted from the source counts. We compare measured vignetting with theoretical vignetting determined in raytrace simulations and find that the two agree to within 10%.

1 Overview

For an on-axis observation, the entirety of the effective area for all 6 HRMA shells contribute to the overall observed source brightness. However, if a source is observed off-axis, the effective area contributing to overall observed source brightness decreases, since the projected area of the mirrors decrease as off-axis angle increases.

Vignetting is the ratio of off-axis to on-axis effective area. Current tables of vignetting values in the CALDB are based on the results of HRMA raytrace simulations. In this memo, we measure vignetting from on-orbit observations at a series of off-axis angles θ and energies. These results can be directly compared with the raytrace results used in the CALDB vignetting tables.

2 Experimental Setup

We utilized a series of off-axis exposures of G21.5, a nearby supernova remnant, to investigate mirror vignetting as a function of off-axis angle. We chose G21.5 because it is a bright source with a well known spectrum which should not be affected by pileup. Exposures were taken at off-axis angles θ of $0'$, $2'$, $5'$, $10'$, $15'$, and $20'$. These exposures correspond, in order of increasing off-axis angle, to obsids 1838-1843. The aimpoint for all these observations was at the S3 aimpoint position, with an additional sim_z offset applied to place the source on the same chip position at each off-axis angle. By consistently placing the source at the same chip position, our observations should be unaffected by spatial variations in quantum efficiency across the detector.

3 Analysis Framework

We calculate 3 useful diagnostic quantities. The first of these we'll label $R_1(\theta)$, a direct measure of vignetting. For a particular off axis angle (θ), sky position (p), aperture size (a), and energy range (Δe), the counts C(Δe) received at the detector is:

$$C(\Delta e) = a \int_{\Delta e} de\ E(\theta, e)\ F(e, p) \tag{1}$$

where E is our exposure map correction and F is the source spectrum. We assume our exposure map correction E is constant over Δe. Then:

$$C(\Delta e) = aE(\theta) \int_{\Delta e} de\ F(e, p) \tag{2}$$

Our exposure map correction consists of three different parts,

$$E(\theta) = V(\theta) A_{\text{eff}} Q \tag{3}$$

a mirror vignetting factor V, effective area A_{eff}, and quantum efficiency Q.

$R_1(\theta)$, the ratio of counts off axis (at some angle θ) vs. on axis is:

$$R_1(\theta) = \frac{C(\Delta e, \theta)}{C(\Delta e, 0)} = \frac{V(\theta)}{V_{on}} \tag{4}$$

For the purpose of calculating $R_1(\theta)$, we consider Q to be a constant at different off axis angles θ, since our exposures were explicitly taken with specific sim_z offsets in order to always place the source on the same spot of the chip. However, source size on the detector will vary when observing the same source at different off-axis angles. To check whether Q is truly constant as a function of off-axis angle, we calculate $R_2(\theta)$ as follows:

We calculate an exposure correction E_2 setting both vignetting and mirror effective area to 1, thus correcting the data only for the difference in detector Q. In other words:

$$E_2 = Q(\theta) \tag{5}$$

Dividing counts by E_2, we get:

$$\frac{C(\Delta e)}{E_2} = V(\theta) A_{\text{eff}} \int_{\Delta e} de\ F(e, p) \tag{6}$$

If we calculate $R_2(\theta)$ like so:

$$R_2(\theta) = \frac{C(\Delta e, \theta)}{E_2(\theta)} \Big/ \frac{C(\Delta e, 0)}{E_2(0)} \tag{7}$$

we should get $R_1(\theta)$ back out. Thus, calculating $R_2(\theta)$ lets us determine whether it is an acceptable approximation to consider Q constant at different off-axis angles.

We calculate a third diagnostic quantity, $R_3(\theta)$, in order to determine how well the full exposure map corrects for off-axis vignetting. In this case, we set E_3 equal to:

$$E_3 = V(\theta) A_{\text{eff}} Q \tag{8}$$

If we calculate $R_3(\theta)$ like so:

Table 1: Summary Table of Observations

Off-Axis Angle θ ()	Obsid	Usable Exposure Time s
0	1838	7854.466
2	1839	7658.579
5	1840	3583.956
10	1841	7999.802
15	1842	–
20	1843	–

$$R_3 = \frac{C(\Delta e, \theta)}{E_3(\theta)} \Big/ \frac{C(\Delta e, 0)}{E_3(0)} \tag{9}$$

we expect to find a value of $R_3(\theta)$ of 1.

4 Data

A summary table of the observations and corresponding off-axis angle is presented in Table 1. A sample spectrum (with power law fit) for the on-axis observation obsid 1838 is presented in Fig. 1.

4.1 Quality of Data

We filtered the data for periods of high background. Lightcurves were calculated from the level 2 event files using a $10'^2$ rectangular region centered $\sim 5'$ from the source. The same region (in celestial coordinates) was used for all obsids. Lightcurves for each obsid and off-axis angle are presented in Fig. 2. Each temporal bin has a length of 200 s.

Obsids 1838, 1839, and 1841 ($0'$, $2'$, and $10'$ off-axis) were taken during periods of low background ($\sim$0.42 counts/s for the entire $10'^2$ region) and can be used with minimal filtering. Periods of high background in obsid 1840 ($5'$ off-axis) require filtering out the entire second half of the observation. Background was consistently high throughout obsids 1842 and 1843 ($15'$ and $20'$ off-axis), rendering these obsids unusable. The total usable exposure time for the $0'$, $2'$, $5'$, and $10'$ off-axis pointings are presented in Table 1. We have requested that the $5'$, $15'$, and $20'$ off-axis pointings of G21.5 be reobserved.

4.2 Building Exposure Maps

For each off-axis angle observation of G21.5, a series of exposure maps was generated for circular regions centered on the source with a radius of $0.71'$. Exposure maps were also generated for a rectangular $10'^2$ background region centered $\sim 5'$ from the source (this is the same region utilized for lightcurve determination). The same source and background regions (in celestial coordinates) were used for each off-axis angle. (For a more detailed discussion of background determination, see §4.3.) A series of exposure maps was generated for 1 keV energy bins covering the 0-10 keV energy band. This energy bin width was chosen in order to assure a high ($\geq$10) signal to noise ratio at energies smaller than 7

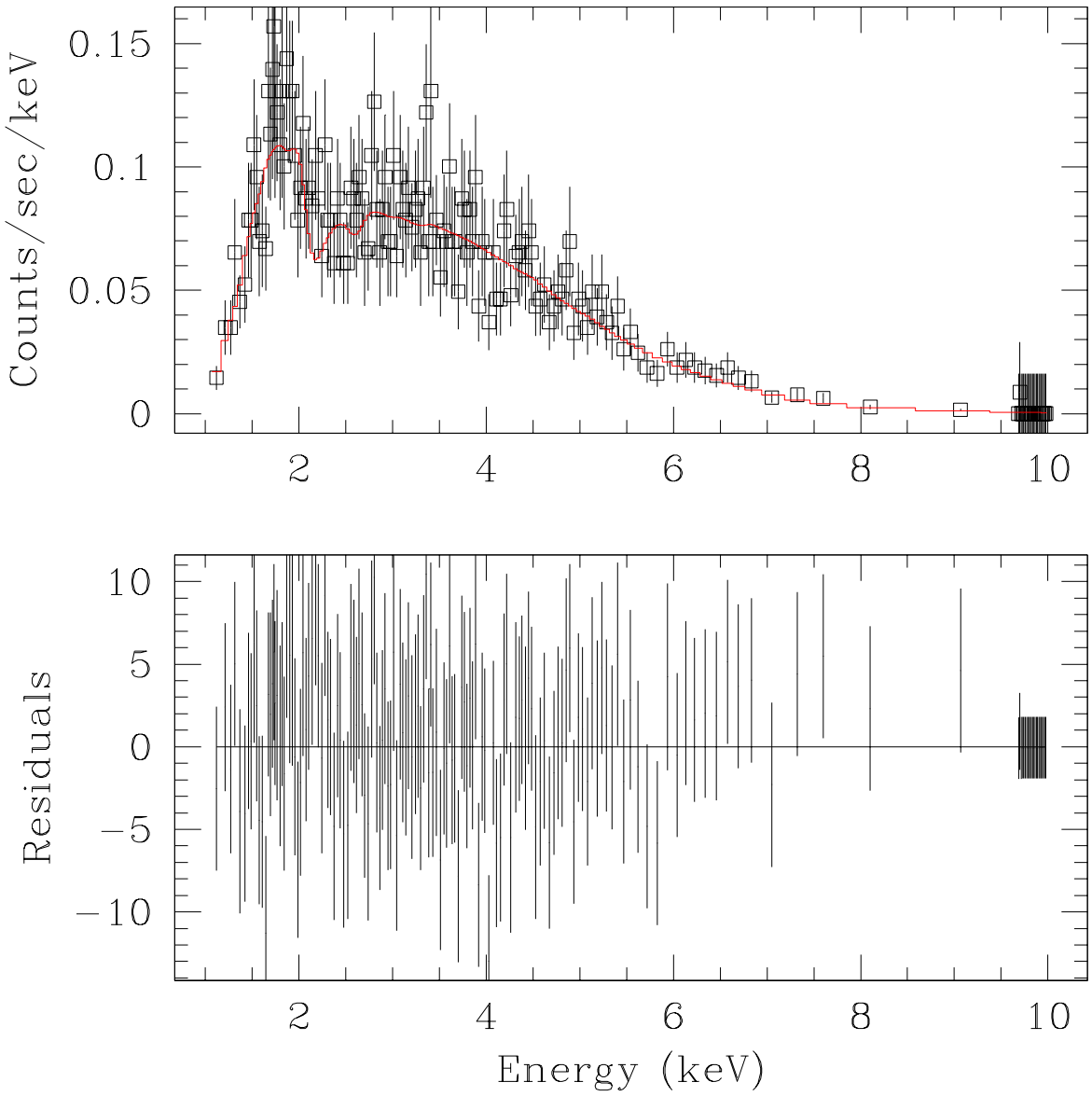

Figure 1: Spectrum of G21.5 On-Axis (obsid 1838). Fit is a power law plus nH absorption.

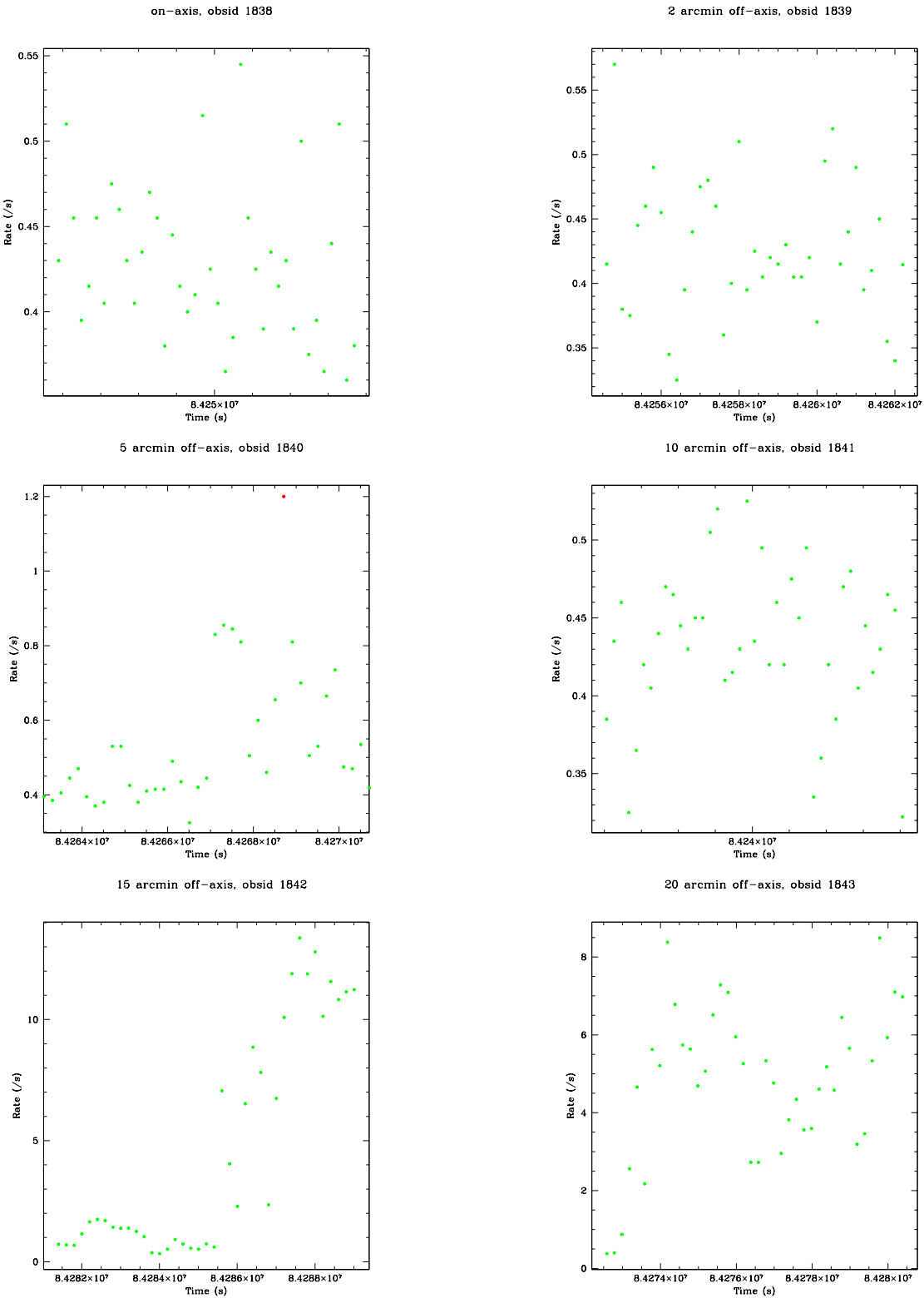

Figure 2: Unfiltered lightcurves for obsids 1838-1843.

keV. Exposure maps were weighted according to a spectral fit of the on-axis observations (obsid 1838, see Fig. 1). Exposure maps were generated for the cases described in §3.

We calculated 3 quantities for each off-axis angle and energy bin (δe):

1) Background subtracted counts (in units of counts/arcsec^2/s):

$$C(\Delta e, \theta) = C_s - \frac{C_b a_s}{a_b} \tag{10}$$

where C_s and C_b are source and background count rates respectively, and a_s and a_b are source and background apertures respectively.

2) Background subtracted counts corrected using E_2:

$$\frac{C(\Delta e, \theta)}{E_2} = \frac{C_s}{E_{2source}} - \frac{C_b a_s}{a_b E_{2back}} \tag{11}$$

3) Background subtracted counts corrected using E_3:

$$\frac{C(\Delta e, \theta)}{E_3} = \frac{C_s}{E_{3source}} - \frac{C_b a_s}{a_b E_{3back}} \tag{12}$$

Dividing each of these 3 quantities at some angle θ by the corresponding quantity at θ=0 gives us $R_1(\theta)$, $R_2(\theta)$, and $R_3(\theta)$ respectively as a function of energy bin. (See §2). Plots of these quantities are presented and discussed in §5.

4.3 Background Issues

We considered two different methods of background determination for this dataset – background subtraction using the ACIS background dataset or using a background extracted off-source from the image itself. We discuss the benefits and pitfalls of each method below. With both, it is impossible to simulate both the sim_z position and off-axis angle used in observing the source.

The ACIS backgrounds were observed on-axis with a negligible sim_z offset. An off-axis region from the ACIS background corresponding to the off-axis angle of the source can be chosen – however, it will not possess the same sim_z offset as our source. While mirror vignetting effects due to off-axis angle will be consistent between source and background, source and background will fall on different regions of the chip. Variation of quantum efficiency across the chip will have to be taken into account between source and background. Not only will background come from a different part of the chip than the source, background will fall at a different chip position for each off-axis angle. Variation of quantum efficiency across the chip will also have to be considered between different backgrounds. Complicating matters further, our background region using this method would fall off of the S3 chip for off-axis angles greater than $5'$. In addition, the ACIS background datasets were observed at different galactic latitudes than our source, and thus, possess a different neutral hydrogen column density than the source.

Instead of using the ACIS backgrounds, background was determined from a rectangular region on the image $5'$ from the source. While backgrounds determined from the image are still at a different off-axis angle than the source, the sim_z offset is the same. Background will come from a different part of the chip than the source, but will consistently fall at the same chip position for each off-axis angle. Quantum efficiency will not vary between different off-axis angle backgrounds. Furthermore, it is always possible to derive a background from the image (no danger of falling off the chip). This leads to a more uniform handling of backgrounds than possible in the ACIS background case. The background will also fall closer to the source for off-axis angles greater than $5'$ than the comparable ACIS background. We expect the background derived from the image to more realistically reflect the background at the source, since it ensures that the value of neutral hydrogen column density is the same in both source

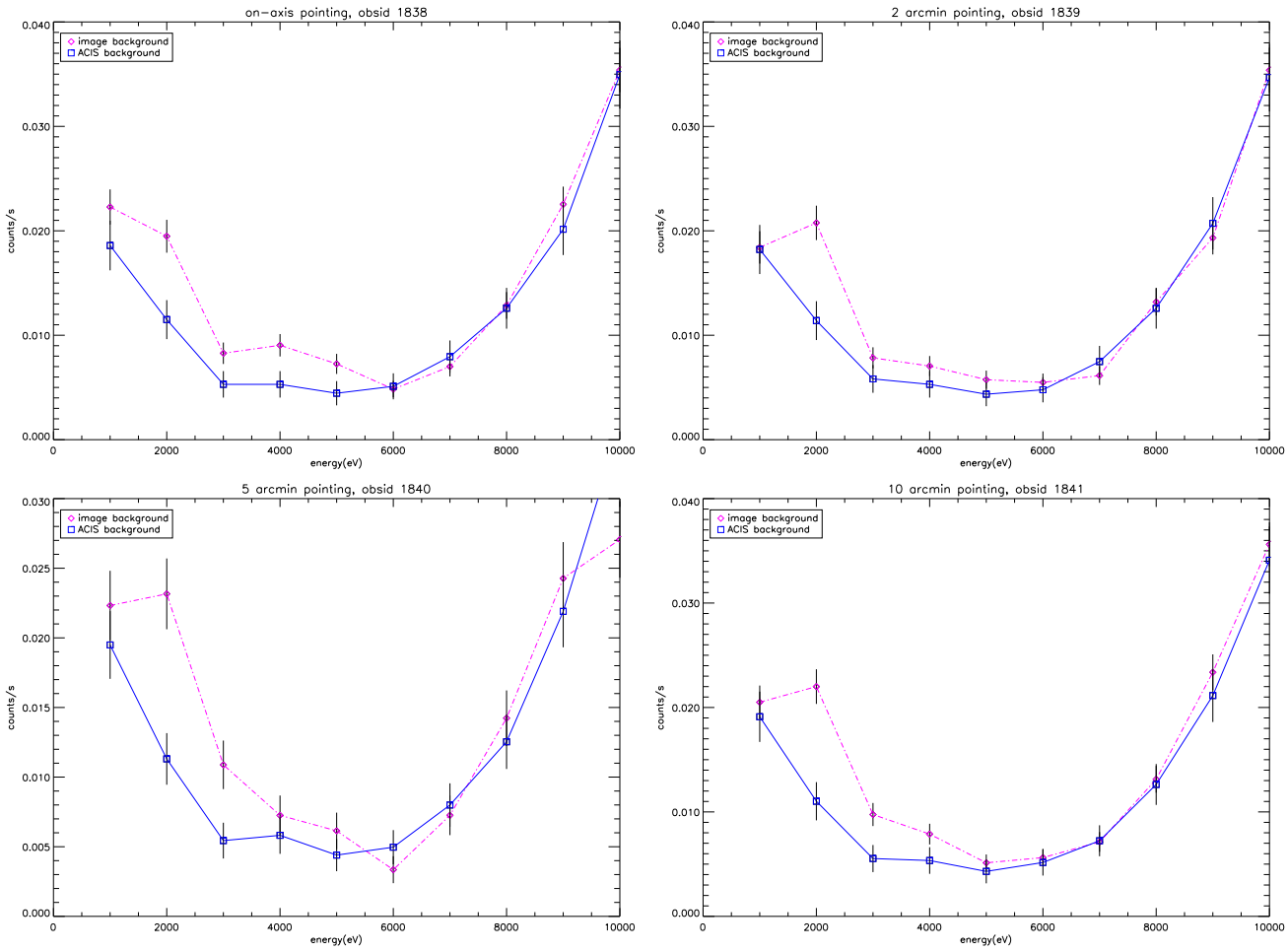

Figure 3: Image backgrounds overlaid on top of an on-axis ACIS background for obsids 1838-1841.

and background. Overall, background derived from the image offer us a less ambiguous measure of vignetting than the ACIS backgrounds.

We compare our image backgrounds to an on-axis ACIS background in order to determine how interchangeable they are (Fig. 3). We find more emission at low energies in the image background, due to differences in galactic nH column between the backgrounds. Overall the backgrounds are similar.

Our backgrounds aren't perfect, but they are adequate for the purpose of background subtraction. Background is still small compared with the source here. We divided the source counts (for all three exposure correction cases) by background counts and plotted the results in Fig. 4. In the energy range of 2000-6000 eV, background is more than 200 times weaker than the source. Thus, background does not contribute noticeably to the total error.

5 Results and Analysis

R_1, R_2, and R_3 are plotted as a function of energy for $\theta = 2$ (Fig. 5), 5 (Fig. 6), and $10'$ (Fig. 7). The ratio of effective areas from raytrace models are also overplotted. R_1 is consistent with the raytrace model ratio within 10% for all three values of θ and energies less than 8 keV. R_2 is universally consistent with R_1, so our assumption of a θ independent Q correction is reasonable. For all three θ's and energies

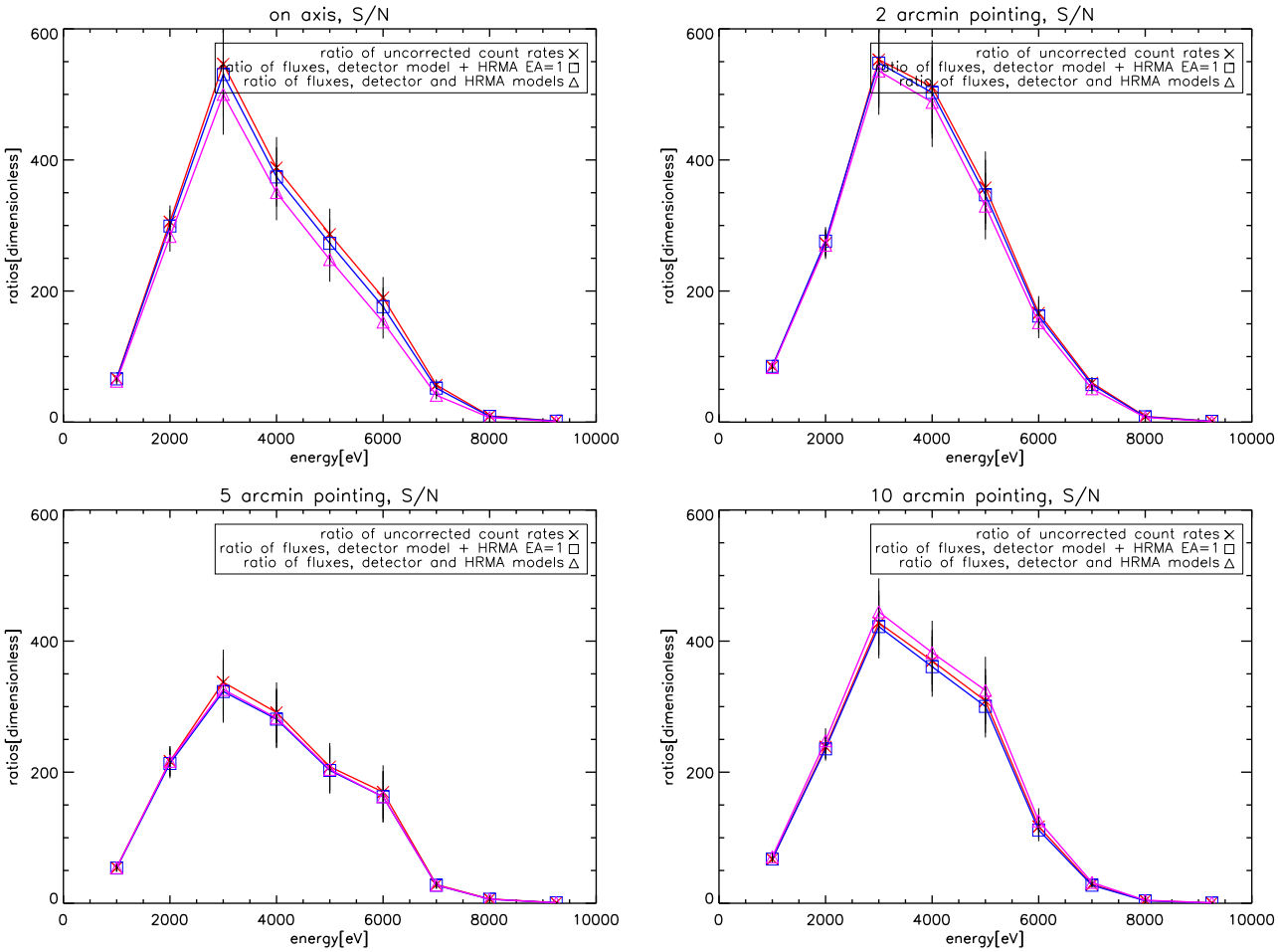

Figure 4: Source Counts divided by Background Counts for obsids 1838-1841.

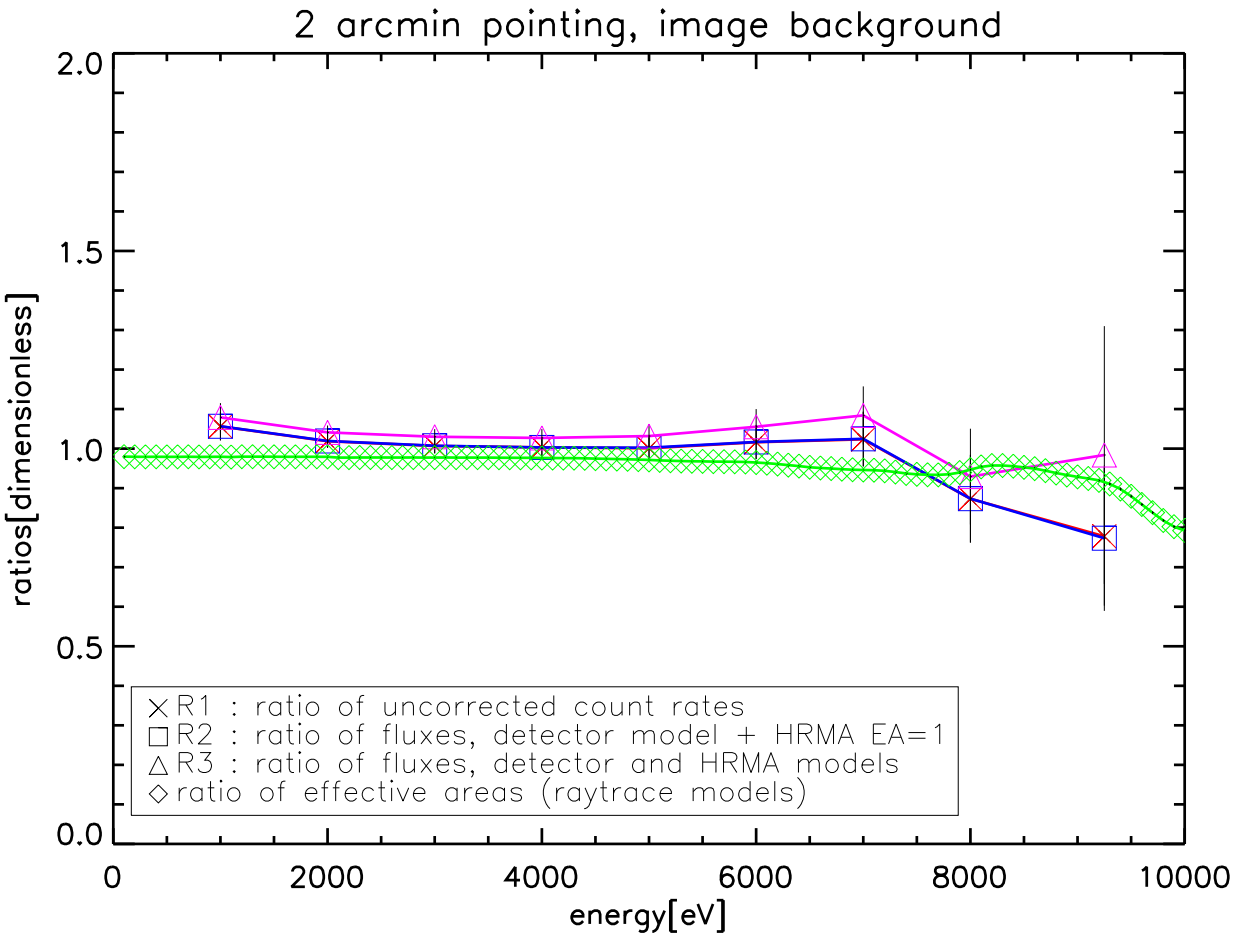

Figure 5: Spectra taken at 2′ off-axis divided by on-axis spectra. R_1 (represented as a cross), R_2 (squares), and R_3 (triangles) are plotted as a function of energy. Background subtraction from image.

less than 8 keV, R_3 is consistent with unity to within 10%.

At higher energies (8 keV and above), the background begins to dominate over source counts. We find larger errors as a result. R_1 and R_2 continue to be consistent with the raytrace model ratio, but within a greater range of uncertainty. R_3 remains consistent with unity, except for the 10 keV point, where it diverges from unity by 50%. Another source of error in these numbers which is not reflected in the error bars is the fact that the background counts were taken from a different off-axis angle than the source counts. To account for this difference in off-axis angle, we are forced to correct the background using the CALDB HRMA vignetting function in order to subtract it from the data. While this affects our result trivially at low energies, where source prevails over background, it is an issue above 8 keV (see Fig. 4), where S/N $\leq$10. These high-energy points cannot be interpreted as vignetting measurements at a single value of θ.

While R_3 is consistent within error to 1, it also seems to mirror the energy dependence of R_1 and R_2. This suggests that we have failed to divide out all the dependence on vignetting.

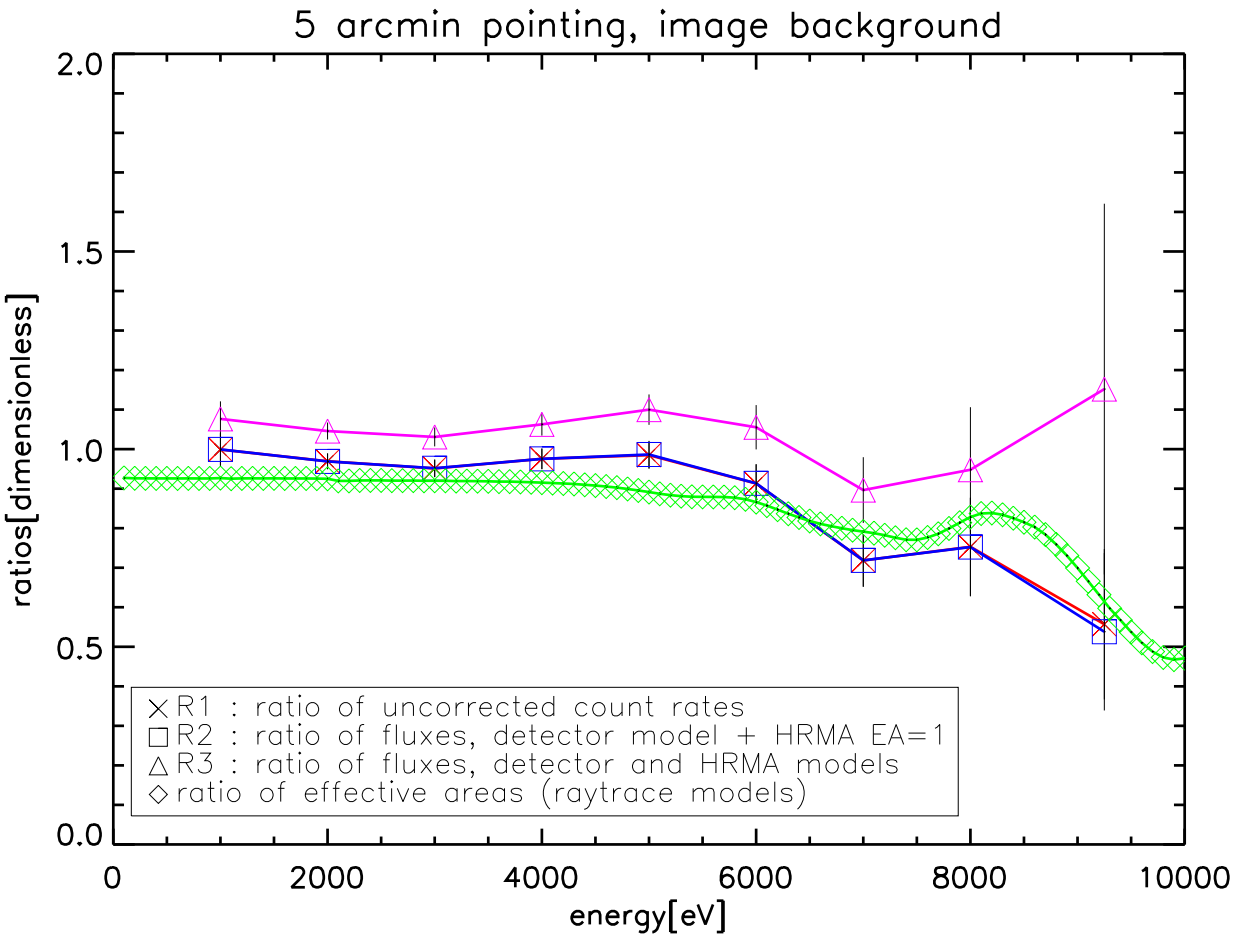

Figure 6: Spectra taken at 5′ off-axis divided by on-axis spectra. R_1 (represented as a cross), R_2 (squares), and R_3 (triangles) are plotted as a function of energy. Background subtraction from image.

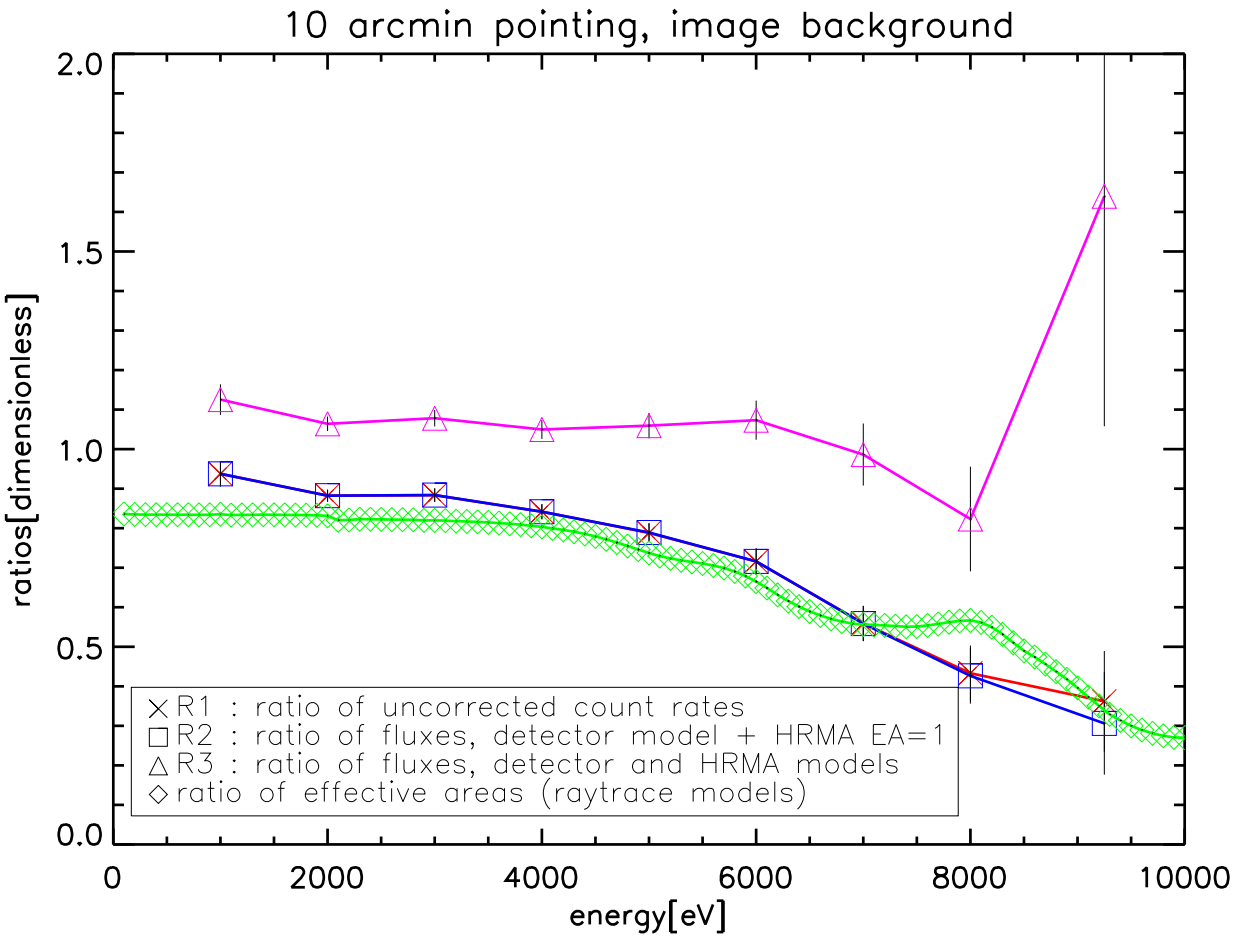

Figure 7: Spectra taken at 10′ off-axis divided by on-axis spectra. R_1 (represented as a cross), R_2 (squares), and R_3 (triangles) are plotted as a function of energy. Background subtraction from image.

6 Conclusions and Further Work

At energies where source brightness prevails above background brightness ($\leq$7 keV), we find that R_1 and R_2 agree to within 10% to the ratio of effective areas from raytrace models for the same θ value. R_3 is consistent with unity to within 10% for these energies.

Since we will be reobserving the $5'$, $15'$, and $20'$ pointings, this work serves only as a preliminary analysis. We suggest a couple methods to improve results for these future observations: 1) longer exposures allowing us to use a finer energy grid. 2) separate background observations. In other words, use the same sim_z offset and off-axis angle, but point at blank sky instead of G21.5. Then use that exposure as a background. This means that high energy points will be believable even if S/N isn't that good, because we are unambiguously using only one off-axis angle.

We calculated estimates of necessary exposure time to produce 20%, 15%, 10% and 5% fractional errors for our 1 keV bins (assuming source and background exposure time are the same and using standard propagation of error.) Estimates were made for each energy bin for which we generated exposure maps, each off-axis angle, and R_{1-3}. Estimates for 20% errors are presented in Table 2. Estimates for 15% errors are presented in Table 3. Estimates for 10% errors are presented in Table 4. Estimates for 5% errors are presented in Table 5.

Our $\sim$8 ksec exposure times easily provide us with $\sim$5% errors for the 1-6 keV bins. Not surprisingly, this is the energy range where signal is highest. In the higher energy bins where signal is lower, the situation is less optimistic – we find $\sim$10% errors for the 7 keV band, $\sim$15% errors for the 8 keV band, and $\geq$20% errors for the 9.25 keV band. To produce $\sim$5% errors for the 7 keV band would require twice as long an exposure. To produce similar errors for the 8 or 9.25 keV energy bands would require 5-10 times as long an exposure.

If we assume that events are spaced evenly within each 1000 eV bin, we can make estimates of necessary exposure time to produce 10% errors for smaller bins. Consider 500 eV bins. If, in each 500 eV bin, we find half the events that we would find in a 1000 eV bin containing the 500 eV bin, then twice the exposure time is needed to produce 10% errors for the 500 eV bin relative to the 1000 eV bin. We find that our exposure time of 8 ksec is adequate to produce $\leq$5% errors for 500 eV energy bins in the 1-6 keV energy range and $\leq$10% errors for 500 eV energy bins in the 6-8 keV range. Exposure times on the order of 40-200 ksec are necessary to produce $\leq$10% errors for the 8-10 keV range.

Table 2: Exposure Times required for fractional errors within 20%

θ (′)	Energy keV	R_1 s	R_2 s	R_3 s
2	1000	220	220	220
2	2000	54	54	54
2	3000	69	69	69
2	4000	93	93	94
2	5000	162	162	162
2	6000	352	352	353
2	7000	890	893	901
2	8000	3135	3195	3349
2	9250	9872	11080	21372
5	1000	223	225	225
5	2000	56	56	56
5	3000	71	71	71
5	4000	95	95	95
5	5000	162	163	163
5	6000	368	368	368
5	7000	1072	1091	1096
5	8000	3191	3372	3461
5	9250	12486	16577	23130
10	1000	234	234	234
10	2000	58	58	58
10	3000	74	74	74
10	4000	102	103	103
10	5000	184	184	184
10	6000	426	427	426
10	7000	1265	1277	1274
10	8000	5220	5486	5233
10	9250	17306	36203	25195

Table 3: Exposure Times required for fractional errors within 15%

θ (′)	Energy keV	R_1 s	R_2 s	R_3 s
2	1000	392	392	392
2	2000	97	97	97
2	3000	123	123	123
2	4000	167	167	167
2	5000	288	288	288
2	6000	627	627	628
2	7000	1583	1588	1602
2	8000	5574	5681	5954
2	9250	17551	19697	37996
5	1000	397	400	400
5	2000	100	100	100
5	3000	126	127	127
5	4000	169	170	170
5	5000	289	290	290
5	6000	654	654	655
5	7000	1906	1940	1949
5	8000	5674	5995	6153
5	9250	22199	29470	41120
10	1000	416	416	417
10	2000	104	104	104
10	3000	132	132	132
10	4000	183	183	183
10	5000	327	327	327
10	6000	758	759	759
10	7000	2250	2271	2265
10	8000	9280	9753	9304
10	9250	30766	64362	44792

Table 4: Exposure Times required for fractional errors within 10%

θ ($'$)	Energy keV	R_1 s	R_2 s	R_3 s
2	1000	882	882	883
2	2000	218	218	218
2	3000	278	278	278
2	4000	375	375	376
2	5000	649	649	649
2	6000	1410	1411	1413
2	7000	3564	3574	3604
2	8000	12542	12783	13397
2	9250	39491	44319	85496
5	1000	894	901	901
5	2000	225	225	225
5	3000	285	285	285
5	4000	382	382	382
5	5000	651	652	653
5	6000	1472	1472	1474
5	7000	4290	4366	4386
5	8000	12767	13488	13845
5	9250	49945	66310	92521
10	1000	936	938	938
10	2000	235	235	235
10	3000	297	297	297
10	4000	411	412	412
10	5000	737	737	737
10	6000	1707	1708	1707
10	7000	5062	5110	5096
10	8000	20880	21945	20935
10	9250	69221	144812	100788

Table 5: Exposure Times required for fractional errors within 5%

θ ($'$)	Energy keV	R_1 s	R_2 s	R_3 s
2	1000	3528	3529	3533
2	2000	874	874	874
2	3000	1113	1113	1113
2	4000	1503	1503	1504
2	5000	2596	2597	2599
2	6000	5643	5647	5655
2	7000	14257	14297	14417
2	8000	50166	51130	53586
2	9250	157959	177271	341998
5	1000	3578	3603	3606
5	2000	900	901	901
5	3000	1141	1143	1143
5	4000	1528	1530	1531
5	5000	2605	2611	2612
5	6000	5890	5890	5896
5	7000	17163	17468	17546
5	8000	51067	53956	55384
5	9250	199776	265254	370071
10	1000	3745	3753	3753
10	2000	941	941	941
10	3000	1190	1191	1191
10	4000	1647	1648	1648
10	5000	2949	2948	2949
10	6000	6828	6835	6832
10	7000	20250	20442	20386
10	8000	83526	87784	83746
10	9250	276904	579280	403156